Supporting Information

for

Superior Performance of an Ultrathin Pyridinic-Layered Micro-Structural Porous Silicon Anode with a Silicon Content Exceeding 99%

Mahesh B. Naikwade, Pranav K. Katkar, *Sang-Wha Lee**

Department of Chemical and Biological Engineering, Gachon University, 1342 Seongnam-daero, Seongnam-si 13120, Republic of Korea.

***Corresponding authors.**

E-mail address: lswha@gachon.ac.kr (Prof. S. W. Lee)

1. Experimental

1.1. Material characterization.

The morphological study of all three samples was carried out by scanning electron microscope (SEM, Hitachi-SU8600, Japan) operated at 5 kV. Phases of the grafted porous silicon in PSi@PyC are investigated by the Transmission Electron Microscope (TEM, Tecnai by FEI, Field Electron and Ion Company, USA) with the energy-dispersive X-ray spectroscopy (EDS) analysis carried out at an acceleration voltage of 300 kV. An X-ray photoelectron spectrometer is used for (XPS Thermo Fisher Scientific, Nexsa). Topology and multi-particle statistics study for evaluating thickness uniformity was conducted by the Atomic Force Microscope (AFM) by Park System XE100 with AFM controller scanned in 3x3 µm in LV mode. The AFM sample preparation in performed in ethanol solvent by the spin coating at 300 RPM on a Si wafer of 2 x 2 cm. XPS data acquisition with the monochromatic source of low-power micro-focused Al Kα radiation (*hv* = 1486.6 eV) at a constant operating voltage of 15 kV. Whereas, full-range XPS spectra are carried out at an energy scan of 50 eV. The obtained XPS data is deconvoluted with XPSPEAK software (4.1 version, Ulvac-PHI, Japan) using Shirley type background and 100,101 Gauss-Lorentzian functions fitting with 80%/20% Gaussian/Lorentzian portion. Raman spectrometer (Monora 500i ANDOR) is operated at 633 nm wavelength to record Raman spectra of all three samples. Detailed investigation of the functional groups and bonding nature within as as-prepared samples are identified by the FT-IR (Bruker Vertex 70, USA). The ATR-FTIR spectra were recorded using a Perkin Elmer Spectrum Two FTIR Spectrometer, which is equipped with a $LiTaO_3$ detector and a PIKE Technologies Miracle™ Universal ATR accessory for single reflection sampling. The carbon content of the m-PSi@PyC is determined in the N_2 atmosphere by the Thermogravimetric analysis (TGA) (SDT Q 600, TA Instrument Germany). The Brunauer-Emmett-Teller (BET) method is used to determine the specific surface area and pore size distribution of the materials using an adsorption analyzer (ASAP 2020 V3, Micromeritics Instrument Corporation, USA). The crystalline phases of the Si in the materials are investigated by the XRD (Rigaku, Japan, Cu K_∞ ($\lambda = 1.5418$ Å) radiation) operated in the 2θ range of 10–90° at a scan rate of 5.0 °/min.

1.2 Calculations:

1.2.1 Kinetics study of Anodic and cathodic reactions:

The CV curves for the m-Si, m-PSi, and m-PSi @PyC at variable scan rates from 0.02 to 0.2 mV s^{-1} are given in **Fig. S6(a-c),** respectively. The redox peak currents obtained from these CV curves of the prepared electrodes are utilized for the detailed kinetics study. The plot of peak current I_p *vs* the square root of scan rate ($V^{1/2}$) as shown in **Fig. S6(d-f)** is given for m-Si, m-PSi, and m-PSi@PyC, respectively. All the plots follow the linear relation with a regression coefficient ranging from 0.93 to 0.99 generally observed for the diffusion-controlled process at early scan rates[1] . The redox peak currents and scan rate follow the following power equations **(S1)** and **(S2)**.[2]

$$i = av^b \tag{S1}$$

$$\log i = \log a + b \log v \tag{S2}$$

Here, v represents the scan rate (mV s^{-1}), i is a peak current (mA), and a and b are the adjustable variables representing a storage mechanism of the anode materials.

1.2.2 Significance of b-values:

The value of b was obtained from the graph of log i vs log v for all the samples as shown in **Fig. S6(g-i).** The b value has a range from 0.5 (a diffusion-controlled mechanism) to 1.0 (a capacitive-controlled mechanism).[3] Here, the b-values for both m-PSi and m-PSi@PyC for anodic and cathodic peak currents lie within 0.6 to 0.80, showing their mixed diffusion and capacitive-controlled Li-ion storage mechanism. Inapposite m-Si obtained b-values of 0.49 and 0.41 (near

0.5) for its anodic and cathodic peak currents, suggesting that a diffusion-controlled Li-ion storage mechanism is prevalent in the m-Si.[4]

1.2.3 Capacity contribution calculation:

The following equations (S3) and (S4) are used for the calculation of the capacitive contribution.[5]

$$i = k_1 v + k_2 v^{1/2} \qquad (S3)$$

$$i/v^{\frac{1}{2}} = k_1 v^{\frac{1}{2}} + k_2 \qquad (S3)$$

Here, k_1 and k_2 are the contribution constants, whereas k_{1v} and $k_2v^{(1/2)}$ indicate capacitive and diffusion current contributions, respectively. The k_1 value is calculated by the slope of $i/v^{1/2}$ *vs* $v^{1/2}$ plot. The individual current contributions for each scan rate are calculated by the following equations, S5 and S6. The percentage of capacitive-controlled current contribution is given by the equation below (S5).[6]

$$\frac{k_1 v}{k_1 v + k_2 v^{\frac{1}{2}}} \times 100 \qquad (S5)$$

Similarly, the percentage of diffusion-controlled current contribution (%) is expressed by equation (S6).

$$\frac{k_2 v^{\frac{1}{2}}}{k_1 v + k_2 v^{\frac{1}{2}}} \times 100 \tag{S6}$$

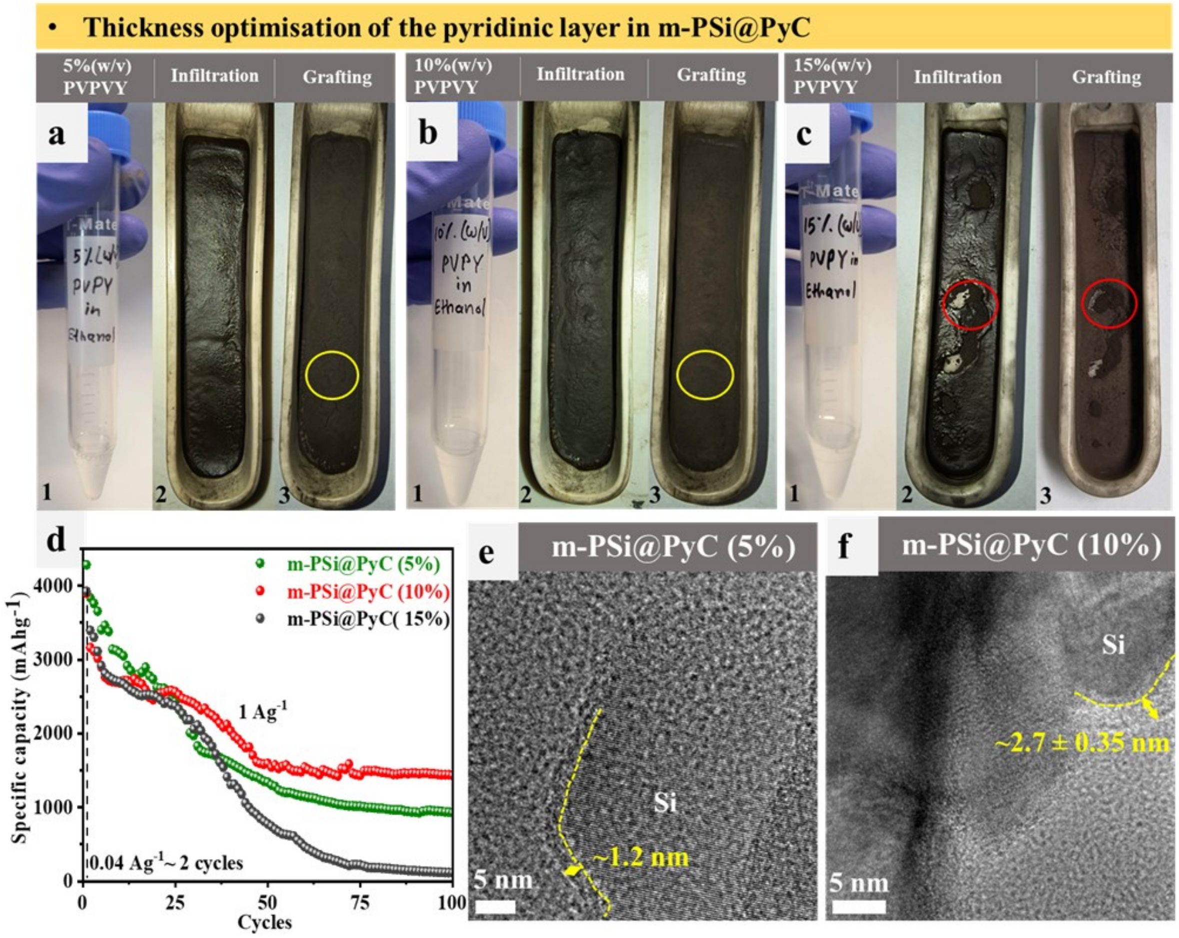

Fig. S1. **Thickness optimization:** photographs of infiltration and grafting procedure for the a) 5%(w/v) PVPY solution, b) 10% PVPY solution, c) 15% PVPY solution, d) cyclic performance of the grafted samples, HRTEM images of the e) m-PSi@PyC (5%) and f) m-PSi@PyC (10%). **Note:** The yellow circled areas in (a)-3 and (b)-3 clearly show a smooth post-grafted surface showing successful grafting. However red circled areas in Figs. (c)-2 and 3 showed incomplete infiltration due to high viscosity and subsequent poor grafting, leaving some portions of the m-PSi exposed at high temperatures.

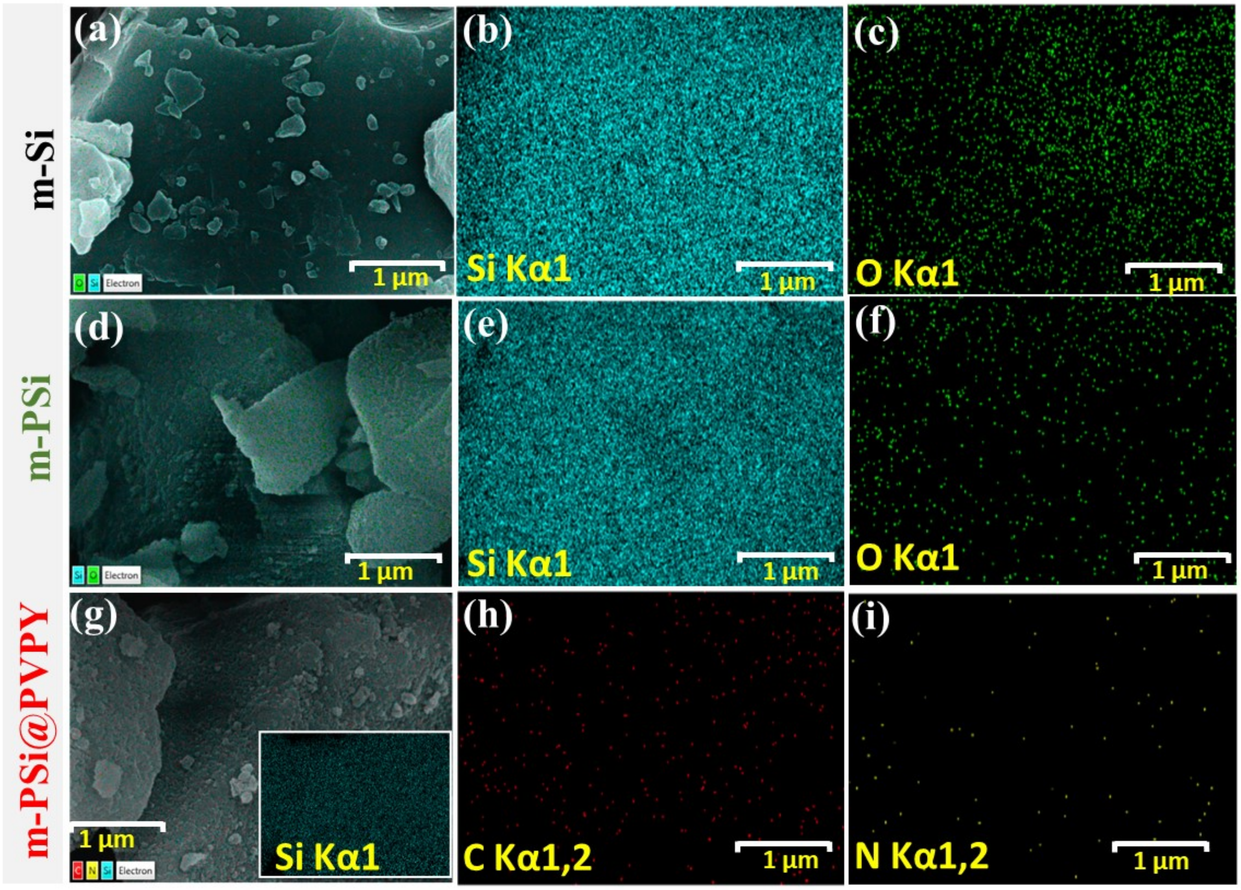

Fig. S2. SEM-EDS mapping of m-Si (a-c), m-PSi (d-f) for Si and O contents and m-PSi@PyC (g-i) for Si, C, and O contents with the respective EDS layered images.

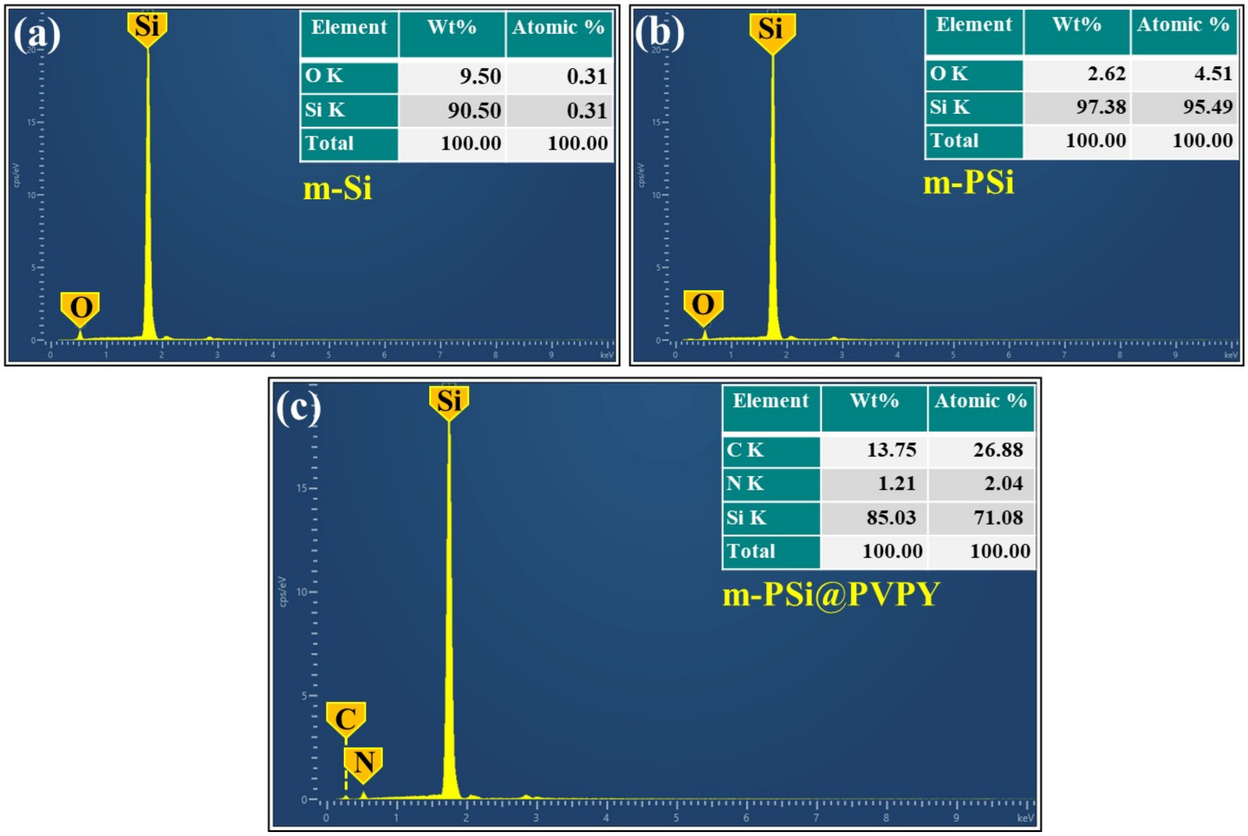

Element	Wt%	Atomic %
O K	9.50	0.31
Si K	90.50	0.31
Total	100.00	100.00

Element	Wt%	Atomic %
O K	2.62	4.51
Si K	97.38	95.49
Total	100.00	100.00

Element	Wt%	Atomic %
C K	13.75	26.88
N K	1.21	2.04
Si K	85.03	71.08
Total	100.00	100.00

Fig. S3. SEM-EDS plots for m-Si (a), m-PSi (b), and m-PSi@PyC (c) for Si, C, and O contents.

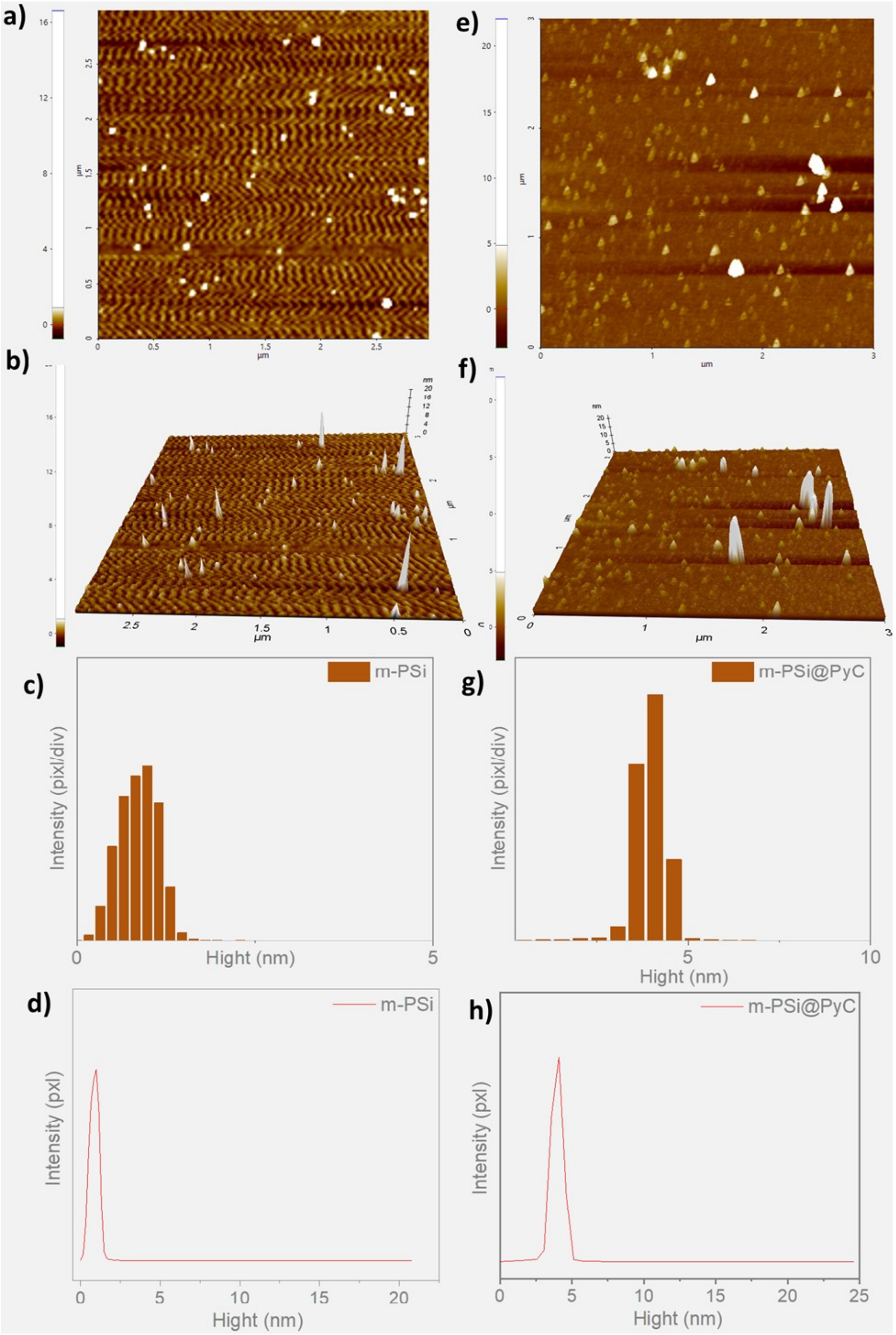
a)
b)
c)
d)
e)
f)
g)
h)
μm
m-PSi
m-PSi@PyC
Intensity (pixl/div)
Intensity (pxl)
Hight (nm)
0
5
10
15
20
25

Fig. S4. (a) AFM image (b)3D AFM image, (c) histogram of particle height distribution, (d) whole region line histogram of the m-PSi, (e) AFM image, (f) 3D AFM image, (g) histogram of particle height distribution, (h) whole region line histogram of the m-PSi@PyC.

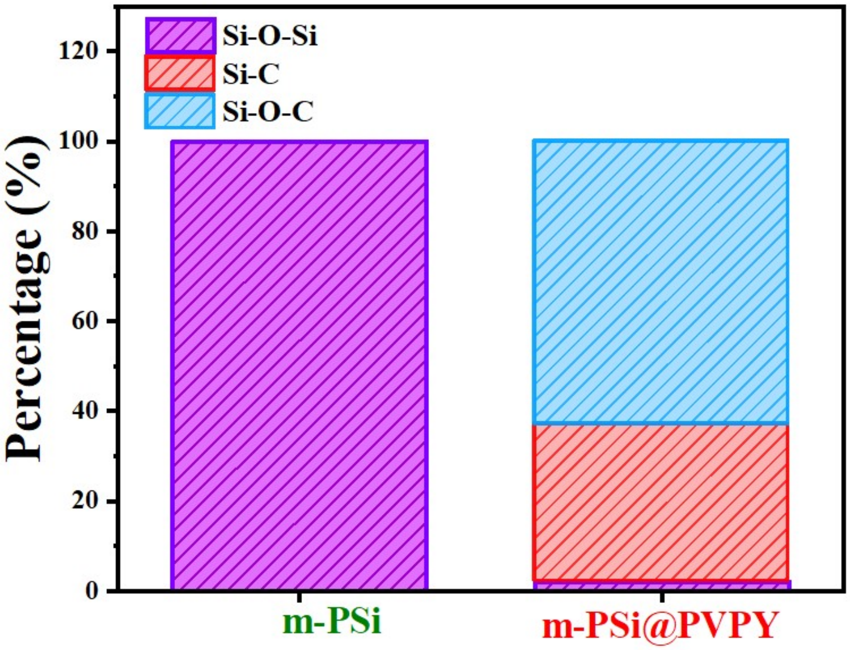

Fig. S5. Surface composition comparison of the samples obtained by deconvoluted XPS Si 2*p* core spectra.

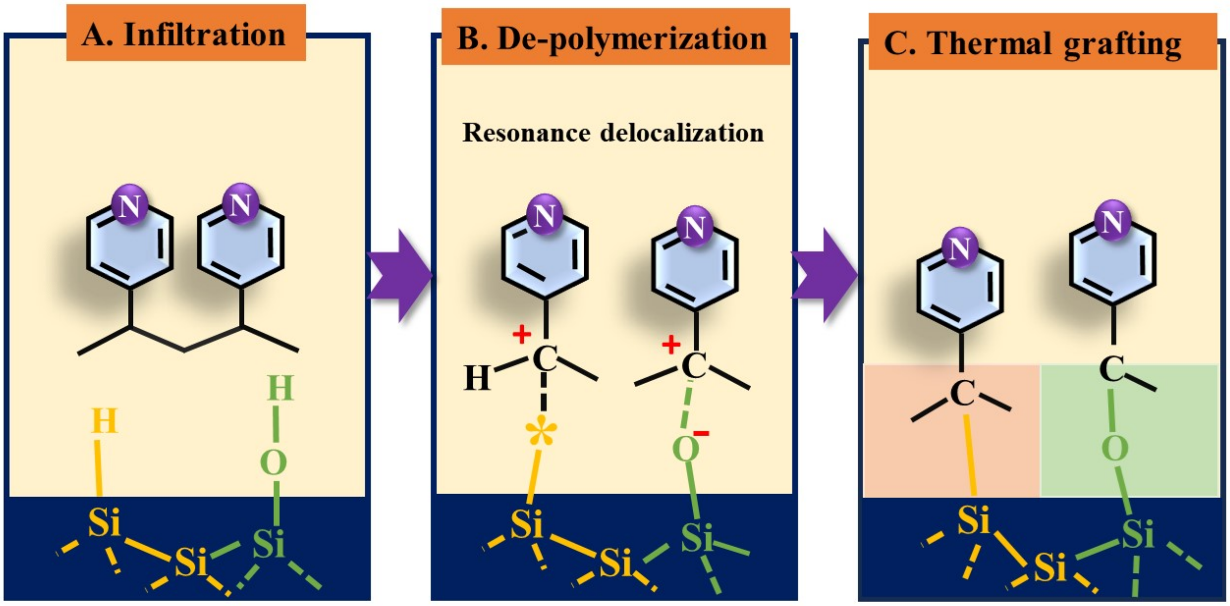

Fig. S6. Plausible thermolytic grafting mechanism for the bonding of pyridinic carbon at the interface of porous silicon composites: A: Infiltration, B: De-polymerization, C: Thermal grafting.

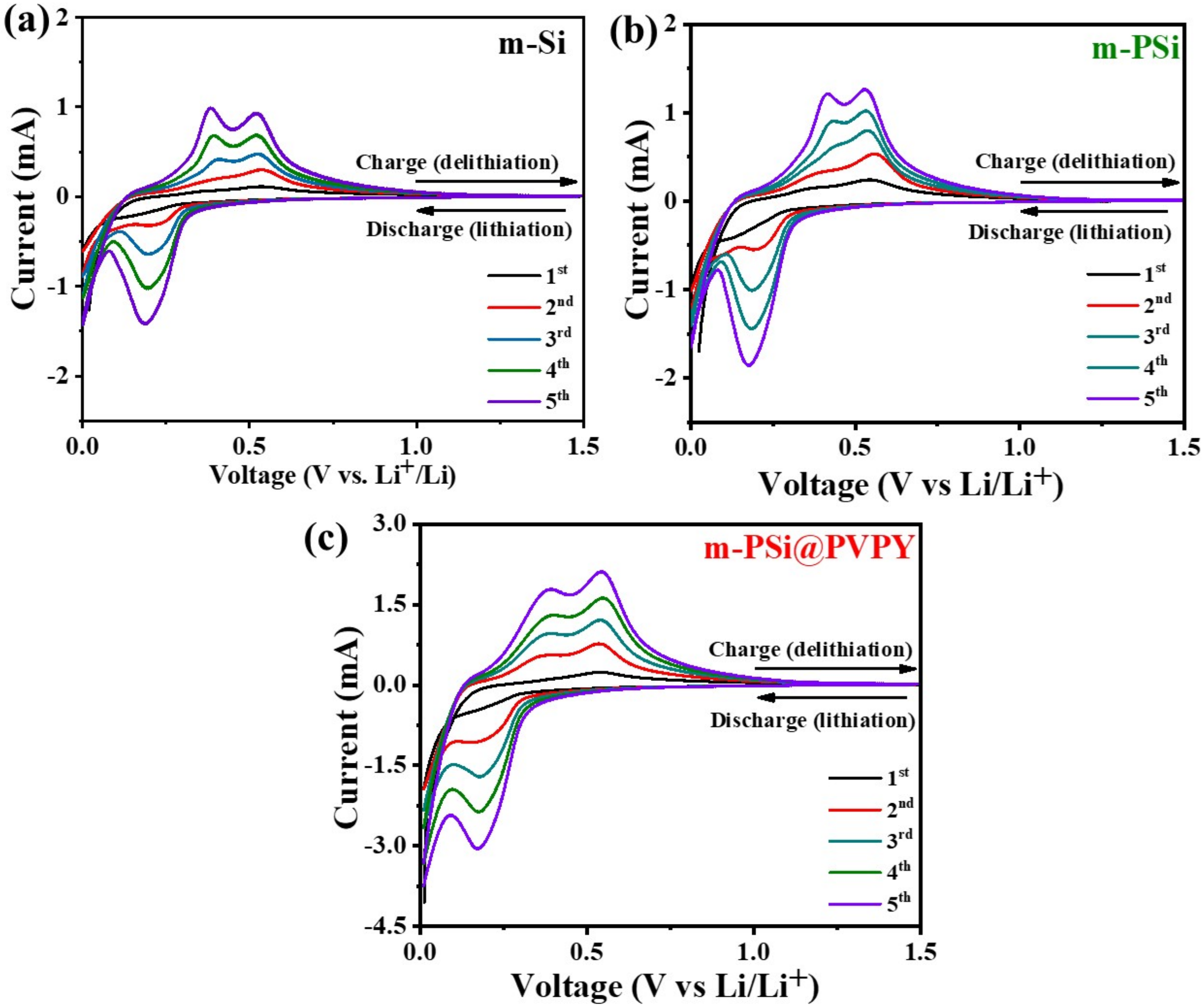

Fig. S7. Cyclic voltammetry curves (CV) for five cycles of (a) m-Si, (b) m-PSi, and (c) m-PSi@PyC.

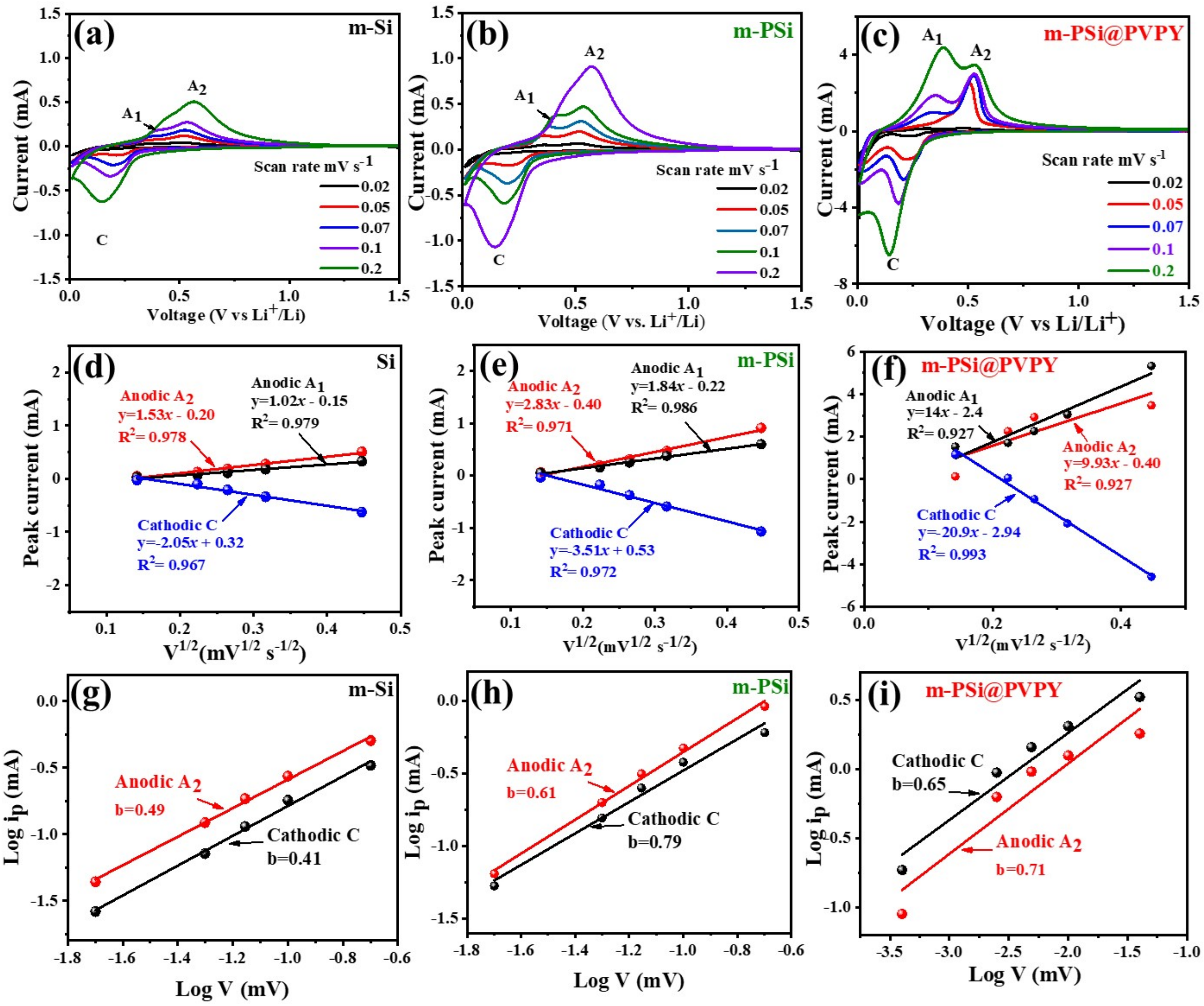

Fig. S8. Cyclic voltammetry (CV) curves of (a) m-Si, (b) m-PSi, and (c) m-PSi@PyC at various scan rates (0.02–2.0 mV s^{-1}), relationship between peak current (i_p) and scan rate (v) plotted in logarithmic axes of (d) m-Si, (e) m-PSi and (f) m-PSi@PyC, corresponding plots of redox peak current density versus square root of scan rate of (g) m-Si, (h) m-PSi, and (i) m-PSi@PyC.

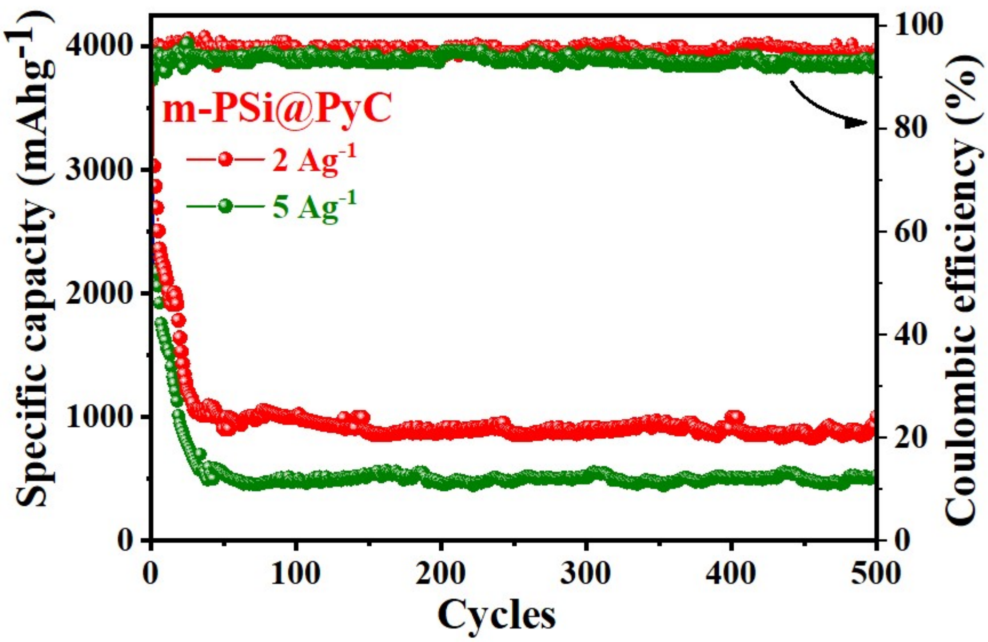

Fig. S9. Long cyclic performance of the m-PSi@PyC at higher current densities of 2 A g^{-1} and 5 A g^{-1}.

Table S1. Cyclic performances and retentions of the m-Si, m-PSi, and m-PSi@PyC samples

Active materials	**5th cycle specific capacity (mAh g^{-1}) at 0.1 Ag^{-1} (After SEI formation)**	**150th Cycle Specific capacity (mAh g^{-1})**	**Capacity retention (%)**
m- Si	2165.16	150.89	6.96
m-PSi	2638.64	1012.56	38.37
m-PSi@PyC	3037.10	2150.82	70.81
Active materials	**5th cycle specific capacity (mAh g-1) at 0.5 Ag^{-1} (After SEI formation)**	**100th Cycle Specific capacity (mAh g^{-1})**	**Capacity retention (%)**
m-PSi	2103.48	718.04	34.13
m-PSi@PyC	2837.10	1720.71	60.65

Table S2. Fitted circuit and the corresponding data of the impedance spectra of Li cells employing the as-prepared samples as anodes before and after 150th cycles

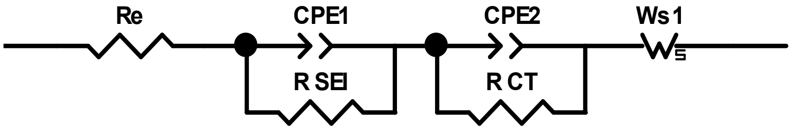

Samples		R_e (Ω)	R_{SEI} (Ω)	R_{ct} (Ω)
m-Si	**Before cycling**	3.90	168.52	158.57
	Post cycling	5.53	352.24	253.23
m-PSi	**Before cycling**	2.39	158.62	108.98
	Post cycling	4.98	242.15	224.48
PSi@PyC	**Before cycling**	1.75	78.25	68.96
	Post cycling	4.65	189.25	170.5

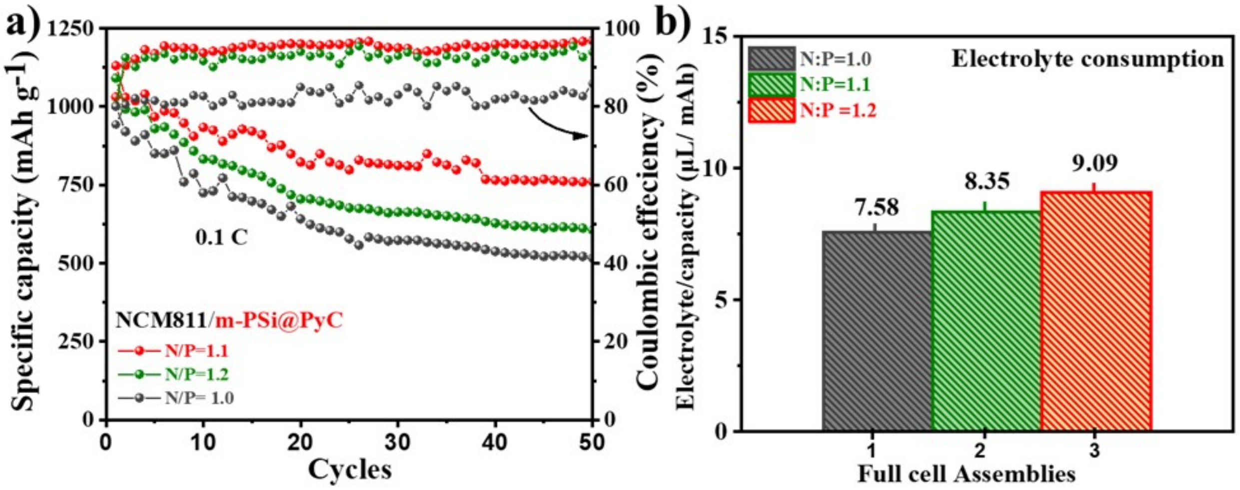

Fig. S10. a) Optimization of the N/P ratio in the NCM811/m-PSi@PyC full cell assemblies b) the electrolyte consumption in the corresponding full cell assemblies.

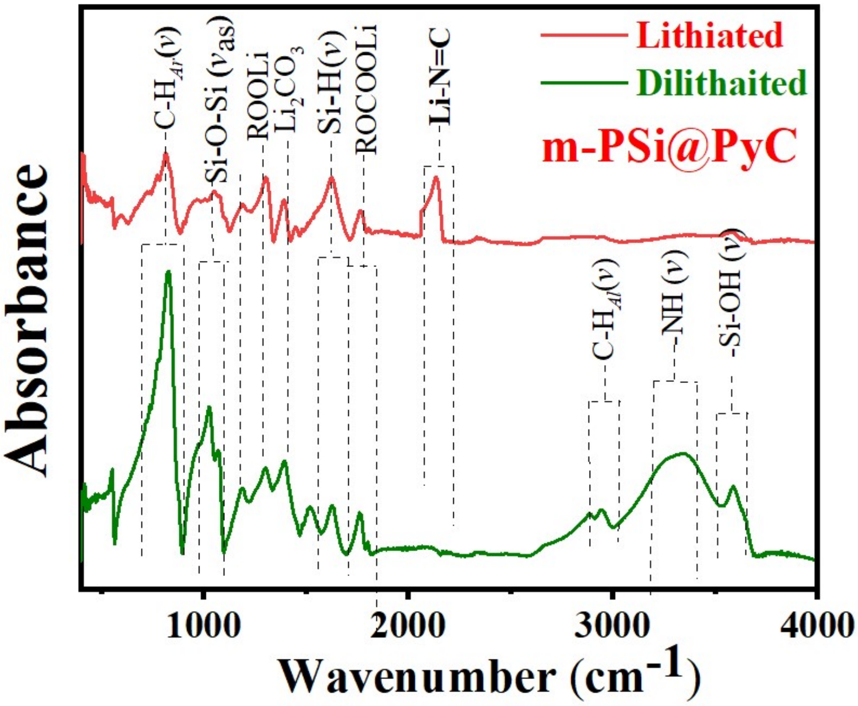

Fig. S11. FTIR Spectra of the lithiated and de-lithiated m-PSi@PyC anode material.

Table S3. Detailed absorption peaks in the Fourier transform infrared (FT-IR) spectra of m-

Observed wavenumber (cm^{-1})	**Peak summary**		**References**
3530-3640	*v*(O-H)	Si-OH	[7]
3200–3600	*v*(N-H)	Hydrogenated Pyridinic or Pyrrolic N groups	[8]
2800–3000	*v* (C-H)	Aliphatic C-H	[9]
2120-2040	***Li-N=C***	Li-N-C(sp^2) species	[10]
1790-1707	*v* (C=O)	Alkyl carbonate ROCOOLi	[11]
1428–1340	*v* (C═O)	Carbonate salt Li_2CO_3	[12]
1223–1342	*v* (O-C–O)	Alkyl carbonate $ROCO_2Li$	[13]
1060–972	*v* (Si–O)	Silicon oxide	[14]
1219–1105	*v*(C–O)	R-CO_2-Li salt	[6]
890–830	*γ* (C–H)	Aromatic carbon (-C_6H_5)	[15]

PSi@PyC composites after lithiation and delithiation

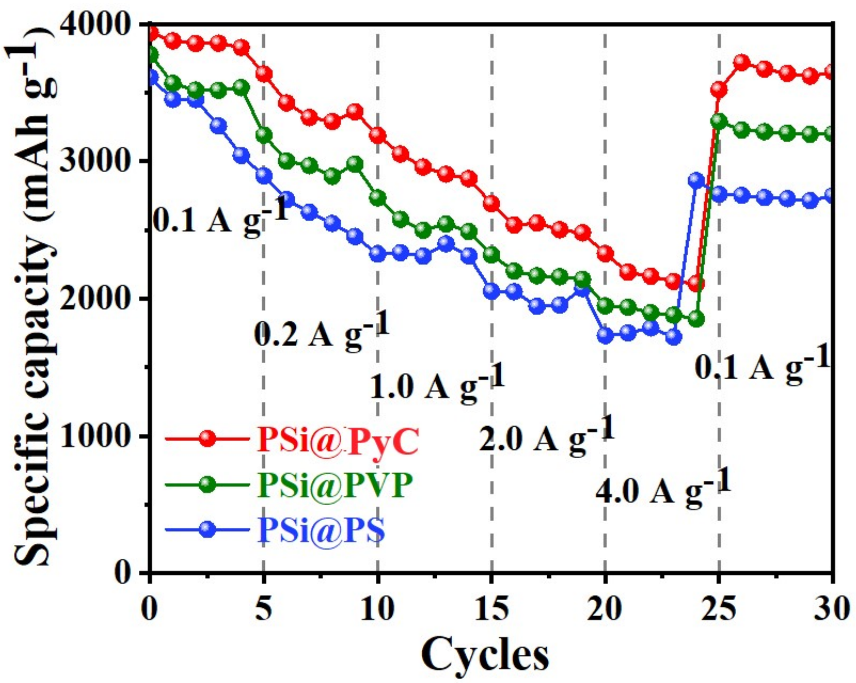

Fig. S12. Rate capability comparison of as-prepared m-PSi and m-PSi@PS samples at a current density ranging from 0.1 A to 4 A g^{-1}.

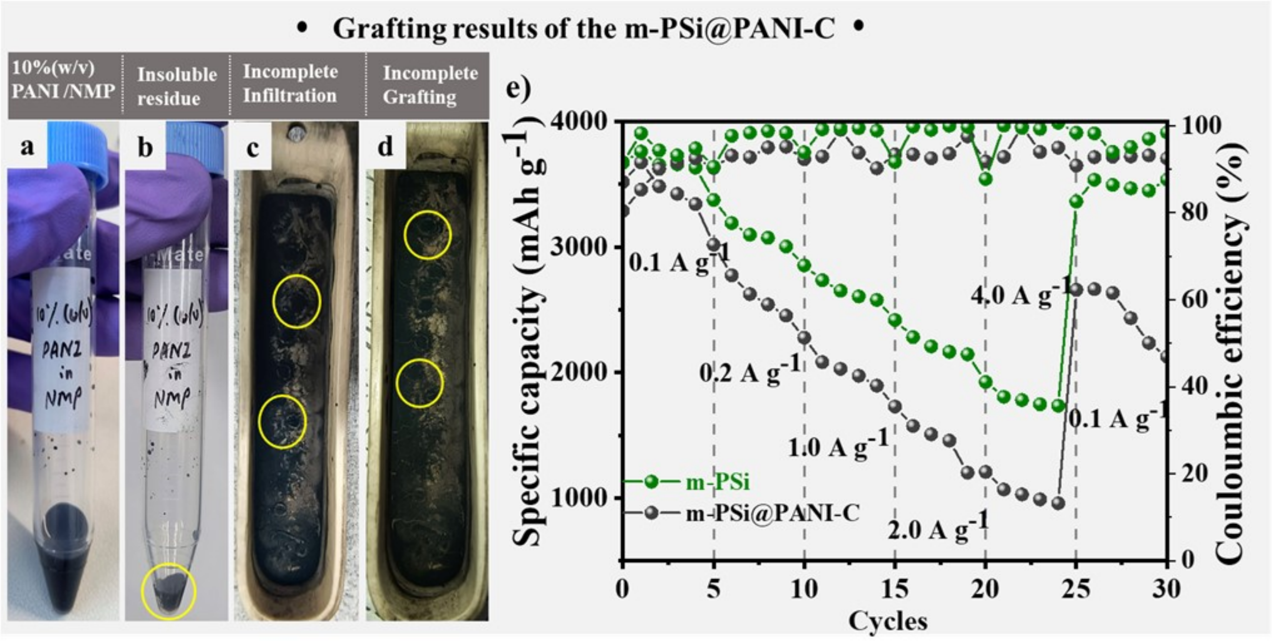

Fig. S13. Grafting results of the m-PSi@PANI-C: a) 10% (w/v) PANI solution in NMP, b) Insoluble PANI residue c) incomplete infiltration of PANI in the m-PSi due to its limited solubility in organic solvents leaving it on the surface as shown in yellow rings d) incomplete grafting causing PANI residues remain ungrafted on the m-PSi surface (yellow ring).

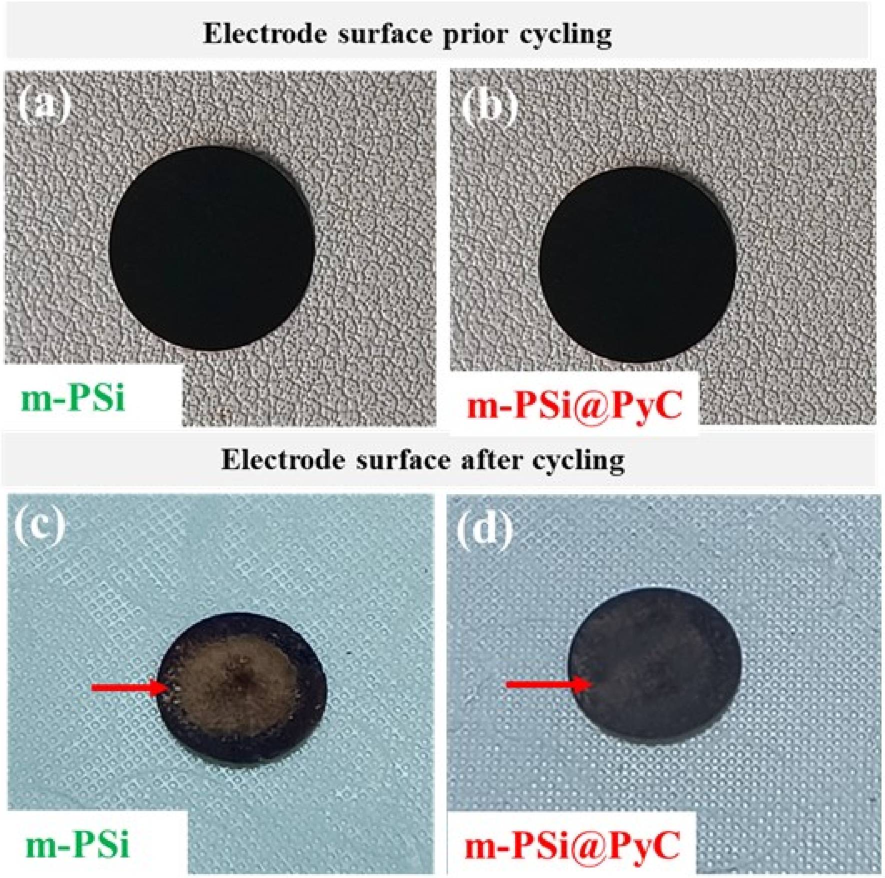

Fig. S14. Prior cycling digital photographs of the electrode surfaces for (a) m-PSi (a) and for (b) m-PSi@PyC, post-cycled digital photographs of the (c) m-PSi and (d) m-PSi@PyC electrodes.

Table S4. Detailed absorption peaks in the Fourier transform infrared (FT-IR) spectra of post-cycled composites

Observed Wavenumber (cm^{-1})	**Peak summary**		**References**
1657–1596	v_{as}(C=O)	Alkyl carbonate ROCOOLi	[11,15]
1550–1531	v (C=O)	Alkyl carboxylate	[15,16]
1453–1350	v (C=O)	Carbonate salt LiO–CO–OLi	[17]
1260–1330	v (C–F)	Fluoroalkyl	[18]
1130–1000	v (Si–O)	Silicon oxide	[19]
950–840	γ (C–O)	Carbonate salt	[20,21]
850–830	v (P–F)	Porous fluorides	[6]
570-526	v (Li–F)	Lithium fluoride	[22]
614–590	v (Si–F)	Lithium hexafluoro silicate	[23]

[*] v: stretching vibration, v_{as}: asymmetric stretching vibration, γ: out-of-plane bending vibration

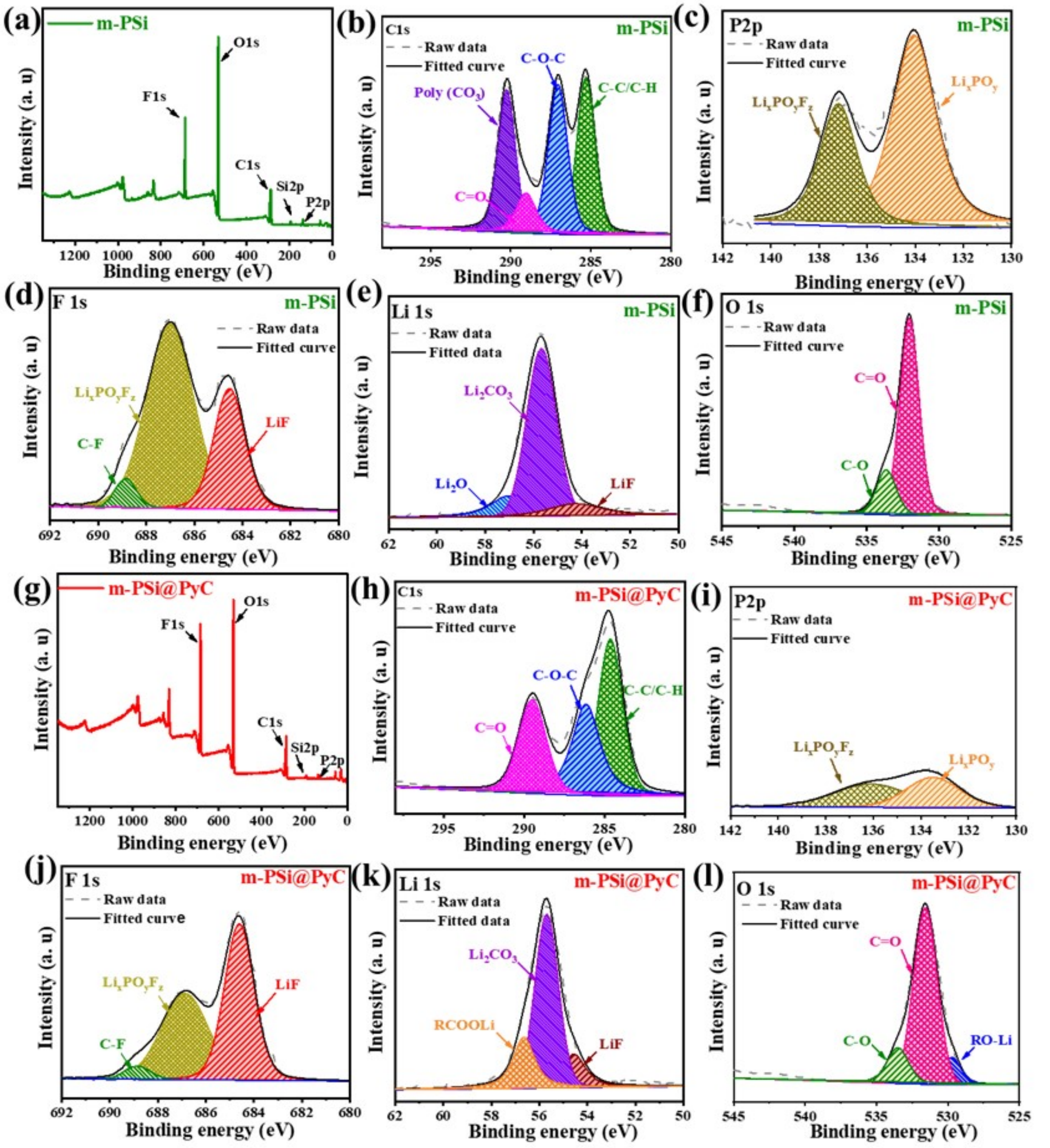

Fig. S15. XPS survey scan of (a) m-PSi, deconvoluted XPS (b) C 1s, (c) P2p, (d) F1s (e) Li 1s, (f) O 1s core spectra of m-PSi, (g) XPS survey scan, (h) C 1s, (i) P2p 1s, (j) F 1s (k) Li 1s, (l) O 1s core spectra of m-PSi@PyC.

References:

1. G. Yang and S.-J. Park, *Sci. Rep.*, 2019, **9**, 4774.
2. J. Chen, Y. Luo, W. Zhang, Y. Qiao, X. Cao, X. Xie, H. Zhou, A. Pan and S. Liang, *Nanomicro Lett.*, 2020, **12**, 1-13.
3. M. Wang, L. An, M. Wu, S. Zhang, Y. Feng, X. Zhang and J. Mi, *J. Electrochem. Soc.*, 2021, **168**, 060510.
4. P. He, Y. Quan, X. Xu, M. Yan, W. Yang, Q. An, L. He and L. Mai, *Small*, 2017, **13**, 1702551.
5. S. Y. Lee, H. Seong, G. Kim, Y. Jin, J. H. Moon, W. Nam, S. K. Kim, M. Yang and J. Choi, *Appl. Surf. Sci.*, 2023, **612**, 155859.
6. M. B. Naikwade, Y. C. Lee, T. T. Salunkhe, I. T. Kim, T.-A. Nguyen, A. Kadam and S.-W. Lee, *ACS Appl. Energy Mater.*, 2024, **7**, 2264-2277.
7. E. Herth, R. Zeggari, J.-Y. Rauch, F. Remy-Martin and W. Boireau, *Microelectronic Engineering*, 2016, **163**, 43-48.
8. Y. V. Fedoseeva, E. V. Lobiak, E. V. Shlyakhova, K. A. Kovalenko, V. R. Kuznetsova, A. A. Vorfolomeeva, M. A. Grebenkina, A. D. Nishchakova, A. A. Makarova and L. G. Bulusheva, *Nanomaterials*, 2020, **10**, 2163.
9. J. D'Angelo and E. Marchevsky, *Part*, 2004, **2**, 34-38.
10. G. M. Veith, L. Baggetto, L. A. Adamczyk, B. Guo, S. S. Brown, X.-G. Sun, A. A. Albert, J. R. Humble, C. E. Barnes and M. J. Bojdys, *Chemistry of Materials*, 2013, **25**, 503-508.
11. D. Aurbach, B. Markovsky, I. Weissman, E. Levi and Y. Ein-Eli, *Electrochimica acta*, 1999, **45**, 67-86.
12. K. Xu, *Chemical reviews*, 2014, **114**, 11503-11618.
13. G. Socrates, *Infrared and Raman characteristic group frequencies: tables and charts*, John Wiley & Sons, 2004.
14. W. Xu, S. S. S. Vegunta and J. C. Flake, *Journal of Power Sources*, 2011, **196**, 8583-8589.
15. M. X. Tran, T.-A. Nguyen, J. K. Lee and S.-W. Lee, *Journal of Power Sources*, 2023, **554**, 232326.
16. D. Aurbach, K. Gamolsky, B. Markovsky, Y. Gofer, M. Schmidt and U. Heider, *Electrochimica acta*, 2002, **47**, 1423-1439.
17. R. E. Ruther, K. A. Hays, S. J. An, J. Li, D. L. Wood and J. Nanda, *ACS applied materials & interfaces*, 2018, **10**, 18641-18649.
18. I. Das and G. De, *Scientific reports*, 2015, **5**, 18503.
19. S. Thombare, R. Patil, R. Humane, B. Kale, R. Kalubarme, D. Malavekar, M. Phadatare and C. Lokhande, *Journal of Materials Science: Materials in Electronics*, 2024, **35**, 1465.
20. F. Du, T. Liao, T. Ye, Y. Wu, G. Guo, K. Zhu, H. Wang, Y. Zhang and Z. Xie, *Journal of Materials Science*, 2022, 1-10.
21. W. Cai, R. Chen, Y. Yang, M. Yi and L. Xiang, *Crystals*, 2018, **8**, 19.
22. J. Wang, G. Gao, X. Zhou, J. Wu, H. Yang, Q. Li and G. Wu, *Journal of Solid State Electrochemistry*, 2014, **18**, 2459-2467.

23. G. Lieser, L. de Biasi, M. Scheuermann, V. Winkler, S. Eisenhardt, S. Glatthaar, S. Indris, H. Geßwein, M. J. Hoffmann and H. Ehrenberg, *Journal of The Electrochemical Society*, 2015, **162**, A679